Enhancing Human Navigation Ability Using Force-Feedback From a Lower-Limb Exoskeleton

Carlos Carrasquillo, Aakash Bajpai, Divya Iyengar, Killian Collins, Anirban Mazumdar, and Aaron J. Young, *Senior Member, IEEE*

***Abstract*—Humans operating in dynamic environments with limited visibility are susceptible to collisions with moving objects, occupational hazards, and/or other agents, which can result in personal injuries or fatalities. Most existing research has focused on using vibrotactile cues to address this challenge. In this work, we propose a fundamentally new approach that utilizes variable impedance on an active exoskeleton to guide humans away from hazards and towards safe areas. This framework combines artificial potential fields with current impedance-based theories of exoskeleton control to provide a comprehensive navigational system that is intuitive for human operators. First, we present the mathematical framework to encode information about the locations of obstacles and the safest direction in which to move. Next, we optimize controller parameters in a series of human-subject experiments. Finally, we evaluate the framework in virtual reality on a set of randomly generated obstacle fields in environments where vision is either fully or partially occluded. Our results suggest that the exoskeleton provides significant separation from obstacles and reduced collisions compared to vision alone in conditions where visibility was limited to less than 1.3 m. Our work demonstrates that force-feedback in parallel with a human can improve overall navigation ability in low visibility conditions.**

***Index Terms*—Artificial potential fields, control hierarchy, exoskeleton, impedance control, navigation, robotics, virtual reality.**

I. Introduction

THE modern industrial workplace is a complex environment that demands the careful interaction of human workers, heavy machinery, robotic agents, and moving objects to ensure worker safety. A combination of human factors, including imperfect communication, limited environmental awareness, and movement inaccuracy can lead to otherwise preventable occupational injuries. According to the U.S. Department of Labor's 2020 data, "contact with objects and equipment" was the #3 cause of work-related deaths and #4 cause of work-related injuries [1]. Motivated by the increasing automation of industrial workplaces, most ongoing research aims to reduce the prevalence of collisions by focusing on a machine-centric approach to collision avoidance. However, this approach does not work if the hazard does not possess machine intelligence and physical autonomy. Instead, a subset of the field has explored utilizing human-centric approaches to collision avoidance, leveraging combinations of visual, auditory, and tactile feedback to enhance workers' situational awareness [2], [3] to improve safety.

Visual feedback on a display has long been the gold standard for communicating easily interpretable cues to humans, but it is not suitable in cases where the visual and cognitive pathways are preoccupied or overloaded. For example, visual displays may be undesirable to construction workers, firefighters, or infantrymen if their vision is obscured by dust, smoke, or dense fog [4], [5]. Furthermore, if an operator's attention is diverted, visual cues can be less effective because they require constant vigilance [6]. Instead, some research has explored the feasibility of using tactile feedback as an alternative channel for information transfer. The most common platforms for this research are vibrotactile devices, which utilize an array of tactors usually placed around the head [7], waist [4], [8], thigh [9], or foot [10] to provide vibratory cues. Although vibrotactile devices have historically been successful in research, they often require specialty, single-purpose hardware that would not otherwise be worn. Furthermore, the perceptibility of the stimulus is largely affected by environmental confounds, the attention of the wearer, and temporal effects that result from repeated or continuous exposure [11]. Finally, vibrotactile signals are heavily attenuated by thick or bulky clothing, which can either decrease the perceptibility of the cues or necessitate a lengthy don procedure.

One rarely explored alternative to traditional vibrotactile methods is force-based feedback mechanisms. Humans are naturally receptive to force-based feedback, and guidance strategies that leverage this have already been successfully demonstrated in research [12], [13]. However, the focus of this research is typically limited to devices acting in series with the human and often requires specialty hardware to be deployed for use. Instead, we explore the potential of providing force-based feedback in parallel with the human body using multi-purpose hardware. Active wearable exoskeletons are a promising platform for

Received 21 May 2024; revised 16 November 2024; accepted 2 January 2025. Date of publication 27 January 2025; date of current version 20 June 2025. This work was supported in part by the National Science Foundation (NSF) National Robotics Initiative (NRI) under Grant 1830498 and in part by National Defense Science and Engineering Graduate (NDSEG) Fellowship. This article was recommended for publication by Associate Editor J. Park and Editor-in-Chief D. Prattichizzo upon evaluation of the reviewers' comments. *(Corresponding author: Carlos Carrasquillo.)*

This work involved human subjects or animals in its research. Approval of all ethical and experimental procedures and protocols was granted by the Georgia Tech Institutional Review Board (IRB) under Application No. H18272.

Carlos Carrasquillo, Aakash Bajpai, Anirban Mazumdar, and Aaron J. Young are with the George W. Woodruff School of Mechanical Engineering, Georgia Institute of Technology, USA, and also with the Institute for Robotics and Intelligent Machines, Georgia Institute of Technology, USA (e-mail: ccarrasquillo3@gatech.edu).

Divya Iyengar and Killian Collins are with the School of Mechanical Engineering, Georgia Institute of Technology, USA.

Digital Object Identifier 10.1109/TOH.2025.3533974

this feedback mechanism, as they are becoming increasingly prominent in the workplace [14], [15] due to their ability to augment joint strength [16], reduce energy expenditure [17], [18], [19], and reduce fatigue [20]. As active exoskeleton technology continues to mature, we seek to develop a generalizable control framework that can be deployed in industrial environments for obstacle avoidance in low visibility conditions, with potential applications to zero visibility conditions. Our method aims to suggestively influence the joint-level dynamics of a human to promote movements away from dangerous zones and to safer areas. This controller would supplement an exoskeleton's existing control framework and act as a safety feature that can be activated (rarely) as needed.

We propose a quasi-impedance control scheme that leverages existing wearable active exoskeleton platforms to help users safely navigate around environmental hazards. We develop and validate this system in an indoor environment with precise localization capabilities and discuss potential extensions of our work that utilize onboard sensing for standalone operation. To the best of our knowledge, this is the first work to use an exoskeleton to provide force-feedback for vision-impaired navigation. **This research provides the following contributions: we (1) present the mathematical framework to compute and apply human-interpretable joint torques for safe and efficient navigation, (2) determine optimal controller parameters through a series of human-subject experiments, and (3) quantitatively evaluate the framework in a virtual reality environment on a set of randomly generated obstacle fields for varying degrees of visibility.**

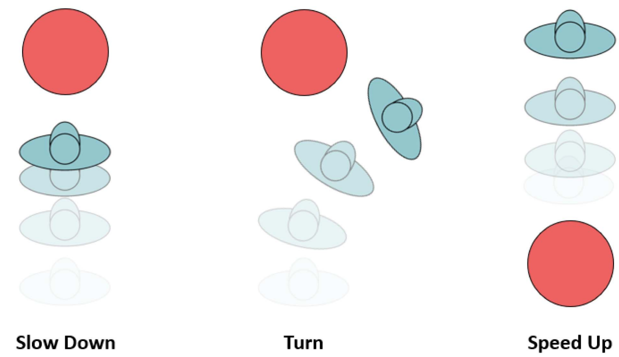

Fig. 1. Human behavior observed during collision avoidance. (Left) The agent decelerates as they approach an obstacle. (Middle) The agent turns to face a safe direction. (Right) The agent accelerates to resume along the path.

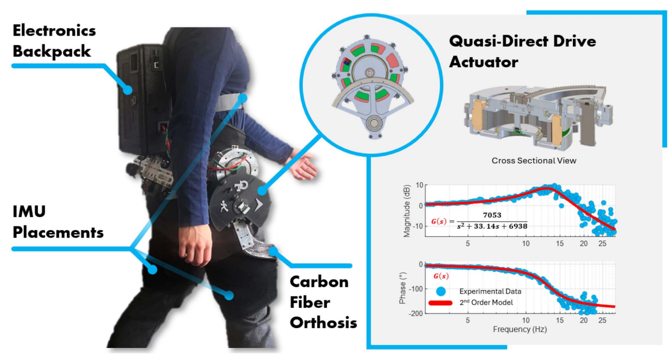

Fig. 2. A close-up of the ARES exoskeleton platform and plots of the actuators' frequency response.

II. Control Architecture

A. Exoskeleton Platform

We evaluated the performance of the proposed control scheme on a 1-DoF exoskeleton. Although a multi-joint exoskeleton has the potential to provide more precise joint-level control, the addition of more active degrees of freedom presents challenges to the size, cost, and weight of these devices. As a result, most multi-joint systems incur energetic costs compared to their single-joint counterparts [21]. Furthermore, the vast majority of commercially viable lower-limb exoskeletons target single degrees of freedom. It follows that if it is possible to demonstrate an efficient navigation communication scheme for a 1-DoF system, it should be possible to extend the paradigm to exoskeleton designs with more control authority.

We characterized human ambulatory navigation as consisting of *translation* and *rotation* motion primitives. In most unconstrained environments, human translation is primarily facilitated by the production of positive power in the sagittal plane, to which the hip and ankle joints are the biggest contributors [22]. Rotation, defined as the alignment of the body to the desired direction of travel, is usually initiated by the hip rotators acting in the transverse plane [23]. During rotation, the external leg necessarily covers a longer path than the internal leg in the sagittal plane, resulting in a change in heading [24]. In both of these primitives, the hip joint's dynamics and kinematics in the sagittal plane play a critical role in the execution of the movement. We therefore selected a sagittal plane hip exoskeleton as the platform for this experiment. In particular, we utilized the Georgia Tech Agile Response Exoskeleton System (GT ARES) for its backdrivability and high torque capability [17].

The GT ARES platform features two brushless quasi-direct drive actuators with a single-stage 10:1 gear reduction ratio (Fig. 2). Each actuator is capable of operating with a continuous (rated) torque of 42.1 Nm, a peak torque of 140.27 Nm, and a zero-load speed of 72.6 r/min. The actuators also exhibit a bandwidth of 20 Hz, a damping ratio of 0.2032, and a peak magnitude of 8.0 dB. The motors are powered by a single 44.4 V 12S battery and are controlled by a set of two Maxon EPOS 50/15 motor controllers featuring low-level PI (P = 1000, I = 1250) torque control. Three Microstrain 3DM-GX5 AHRS IMUs are placed on each thigh and the torso to estimate hip joint angles. The exoskeleton is controlled by Raspberry Pi 4, which is stored in the electronics backpack. The exoskeleton assembly weighs 12.5 kg. We used this device as a test-bed for our approach, allowing us to examine a large trade-space of interaction torques. Once the joint torques are understood an optimized, a lighter exoskeleton could be used.

B. Exoskeleton Control

For local and sudden collision avoidance, pedestrians have been observed to slow down to avoid a collision, turn away from the obstacle, and increase their speed along the planned path (Fig. 1) [25]. The controller was designed to alter the

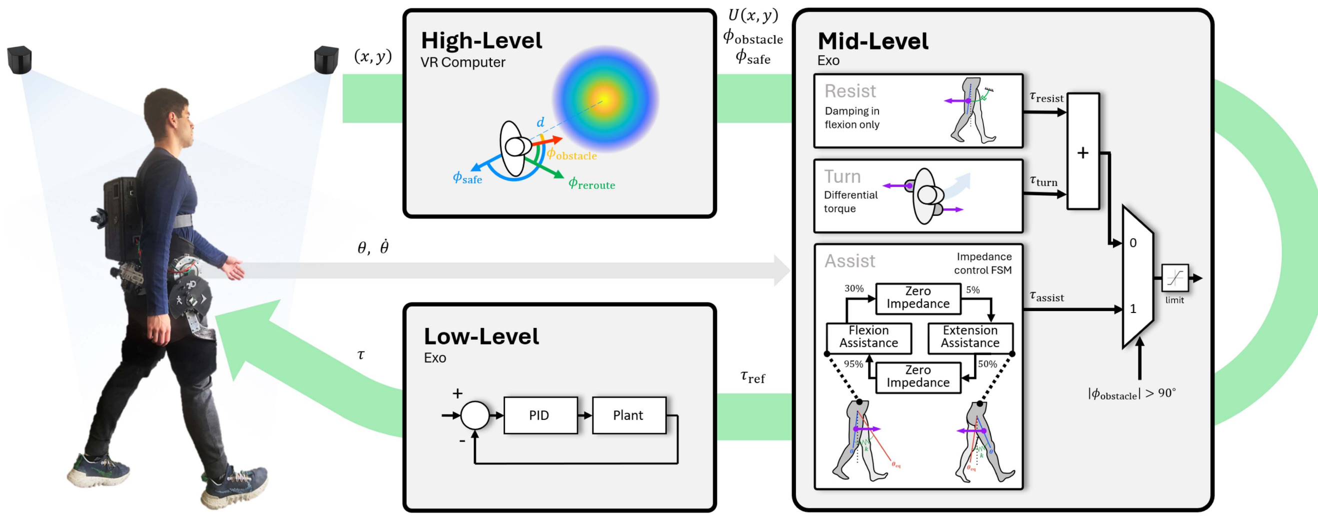

Fig. 3. A diagram of the control hierarchy. State transition criteria in the assistive controller are expressed as a percentage of the gait cycle.

dynamics and kinematics of wearers to artificially induce this behavior. Specifically, the exoskeleton control paradigm consists of three independent behaviors: (1) apply resistance if the wearer is moving towards an obstacle, (2) turn the wearer away from the obstacle, and (3) assist the wearer as they move away from the obstacle. These behaviors were implemented as independent exoskeleton controllers, each of which outputs a reference torque. The reference torques were then summed to obtain an aggregate reference torque, τ_{ref}, which was commanded to the motor controllers (Fig. 3).

1) Resistive Controller: A small amount of damping was applied to the hip joint, intended to replicate the feeling of treading through a dense liquid medium. Damping was only enabled during hip flexion for safety. The output torque of the resistive controller was computed using (1), where m is the user's mass, β is the mass-normalized damping coefficient, $\dot{\theta}$ is the measured hip angular velocity, and $c_1(d) \in [0, 1]$, $c_2(\phi_{\text{obstacle}}) \in [0, 1]$ are scaling factors that depend on the distance to the obstacle d and the heading to the obstacle $\phi_{\text{obstacle}} \in [-180^\circ, 180^\circ)$, respectively. The hip angle θ was measured by subtracting the pitch of a thigh-mounted IMU from that of a torso-mounted unit. θ was tared at startup. The controller acted independently on each leg. This controller was only active when the wearer was walking toward an obstacle (i.e., $|\phi_{\text{obstacle}}| < 90^\circ$).

$$\tau_{\text{resist}} = m \left[\beta\dot{\theta}\right] c_1 c_2 \tag{1}$$

2) Turning Controller: During turning, an equal and opposite torque was applied on both legs. The wearer was instructed to pivot about the leg receiving the extension torque and turn with the leg receiving the flexion torque. The torque was intended to replicate the observed effect of swinging the outer leg more than the inner leg during turning and is similar to pure rotation in differential drive vehicles like tracked robots. The output torque of the turning controller was computed using (2), where τ_{diff} is the maximum mass-normalized torque output of the controller (achieved when the wearer's heading is opposite to the safe direction) and $c_3(\phi_{\text{safe}}) \in [-1, 1)$ is a scaling factor that depends on the angle between the user's heading and predetermined safe heading, $\phi_{\text{safe}} \in [-180^\circ, 180^\circ)$. This controller was only active when the wearer was walking toward an obstacle (i.e., $|\phi_{\text{obstacle}}| < 90^\circ$) and thus acted in tandem with the resistive controller.

$$\tau_{\text{turn}} = \begin{cases} m\,[\tau_{\text{diff}}]\, c_1 c_3 & \text{if leg} = \text{L} \\ -m\,[\tau_{\text{diff}}]\, c_1 c_3 & \text{if leg} = \text{R} \end{cases} \tag{2}$$

3) Assistive Controller: A quasi-stiffness state machine-based impedance controller modeled after the hip's kinematics and dynamics for level-ground walking at the target speed of 1.25 m/s. This model takes advantage of the observation that the hip exhibits sprint-like dynamics during level-ground walking at the target speed [26]. The state machine was designed to have two active states (flexion and extension) and two passive zero-impedance states (Fig. 3). To compute the impedance control mass-normalized spring coefficients, k, and hip equilibrium angles, θ_{eq}, the hip's biomechanics were first obtained from one of our large datasets [27] and averaged across all subjects (N=22) and strides. k and θ_{eq} for flexion and extension were then computed based on the averaged torque-angle relationship. The estimated hip angle θ and θ_{eq} were expressed as a percentage of the range of motion (% ROM) to account for variance in step kinematics. The ROM was computed in real-time by applying a peak detection algorithm on θ. The output torque of the assistive controller was computed using (3), where $\alpha \in [0, 1]$ is the contribution of the spring term as a percentage of biological torque. $c_4(\phi_{\text{safe}}) \in [0, 1]$ is a scaling factor that depends on the heading to the safe direction, ϕ_{safe}. The controller acted independently on each leg. This controller was only active when the wearer was walking away from an obstacle (i.e., $|\phi_{\text{safe}}| < 90^\circ$).

$$\tau_{\text{assist}} = m\left[\alpha k\left(\theta - \theta_{eq}\right)\right] c_1 c_4 \tag{3}$$

C. Navigation Algorithm

We desired a guidance strategy that allows the wearer to retain most of their planning and decision-making authority while communicating intuitive information about how to best evade environmental hazards. Artificial Potential Fields (APFs) offer a computationally inexpensive solution to this problem by decomposing the environment into attractive and repulsive fields. In this paradigm, the human is subjected to a repulsive potential from obstacles while self-selecting their attractive potential to a goal. The safe direction, ϕ_{safe}, was therefore defined as the angle between the wearer's heading and the negative gradient of the repulsive field, $-\nabla U(x, y)$, where x and y are the planar coordinates of the wearer in the field. Similarly, ϕ_{obstacle} was defined as the angle between the wearer's heading, ϕ, and the projection of $\nabla U(x, y)$ onto the X-Y plane. The scaling factor $c_1(d)$ was defined as the magnitude of the repulsive potential, $U(x, y)$.

III. Parameter Optimization

Potential field and exoskeleton parameters have not been previously identified for our application. Due to the large number of parameters in both the exoskeleton controller and the APF, obtaining a globally optimal parameterization via human-in-the-loop testing was deemed experimentally intractable. Instead, parameters for the three mid-level controllers were selected independently and the resulting exoskeleton controller was utilized to select optimal potential field parameters.

A. Exoskeleton Control

To ensure subject safety and maximize controllability, the exoskeleton torque was limited to a maximum of 0.5 Nm/kg. This allows users to easily overpower the exoskeleton in the event of a disagreement.

1) Resistive Controller: Because the resistive and turning controllers are active at the same time during the evasion maneuver, a budget of 0.25 Nm/kg was allocated to each. β was therefore computed by dividing the mass-normalized torque budget by a conservative estimate of the maximum $\dot{\theta}$ during a level-ground, 1.25 m/s gait cycle [27]. $c_2(\phi_{\text{obstacle}})$ was defined as the cosine of ϕ_{obstacle} such that the scaling factor is 1 when the wearer is facing the obstacle and 0 when the wearer's heading is perpendicular to the obstacle (4).

$$c_2(\phi_{\text{obstacle}}) = \cos(\phi_{\text{obstacle}}) \tag{4}$$

2) Assistive Controller: α was computed by dividing the mass-normalized torque budget by a conservative estimate of the maximum mass-normalized torque output of the hip's level-ground, 1.25 m/s impedance model [17], [27]. $c_4(\phi_{\text{safe}})$ was defined as the cosine of ϕ_{safe} such that the scaling factor is 1 when the wearer is facing the safe direction and 0 when the wearer's heading is perpendicular to the safe direction (5).

$$c_4(\phi_{\text{safe}}) = \cos(\phi_{\text{safe}}) \tag{5}$$

3) Turning Controller: The turning controller demanded a scaling factor $c_3(\phi_{\text{safe}})$ that maps the range of heading errors, $\phi_{\text{safe}} \in [-180^\circ, 180^\circ)$, to $[-1, 1)$. Early pilot experiments suggested that defining $c_3(\phi_{\text{safe}})$ using a linear function resulted in a large range of low torque magnitudes at low values of ϕ_{safe} that were difficult for subjects to distinguish. To overcome

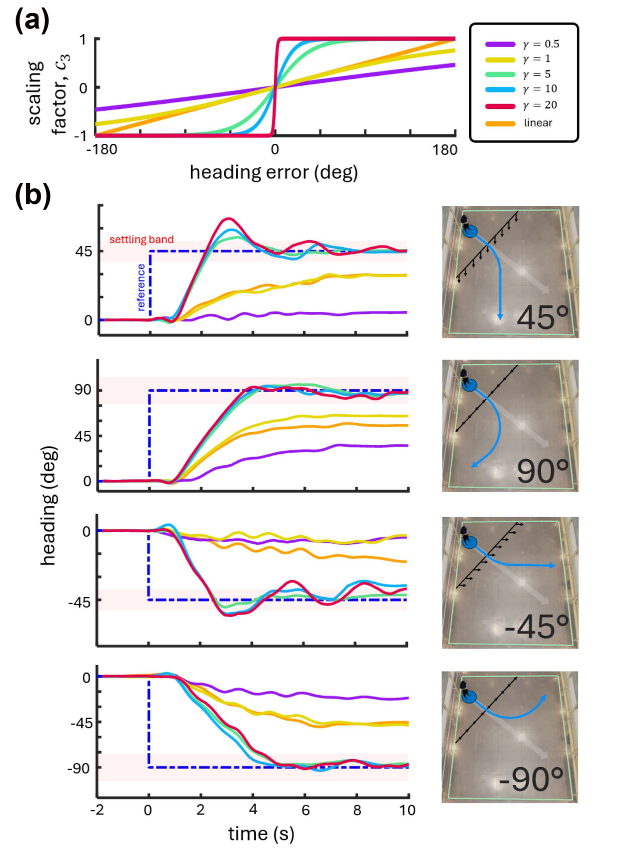

Fig. 4. (a) Candidate functions that map heading errors to a scaling factor, to be used to compute the turning controller's output torque. (b) 45, 90, -45, -90-degree step response plots of a wearer's heading after applying candidate turning controllers. Data were resampled at 100 Hz and averaged at each timestep across subjects (N = 5) and trials (M = 3). A moving average filter of size 40 ms was applied to each trial for plotting purposes.

this problem, we used the hyperbolic tangent function (6). The shaping parameter γ dictates the shape of the torque-error relationship. The larger the γ, the more the control scheme resembles bang-bang control (Fig. 4(a)).

$$c_3(\phi_{\text{safe}}) = \tanh\left(\gamma \frac{\phi_{\text{safe}}}{180^\circ}\right) \tag{6}$$

The candidate turning controllers were evaluated by analyzing the heading step response of wearers subjected to a change in ϕ_{safe} . Subjects were positioned at one corner of an 8 x 8m field and outfitted with the exoskeleton and a VIVE tracker, used to obtain the subject's real-time coordinates. Subjects were asked to walk in a straight line until a step of either -90, -45, 45, or 90 degrees was commanded. These step angles were selected to capture the system's response to varying heading changes, with 45-degree turns representing moderate redirections and 90-degree turns indicating more substantial reroutes. The subject's heading throughout the trial was logged. Trials were randomized across ϕ_{safe} and candidate controllers.

Data were resampled at 100 Hz and averaged at each timestep across subjects (N=5) and trials (M=3). The controller with $\gamma = 5$ consistently achieved among the lowest settling times

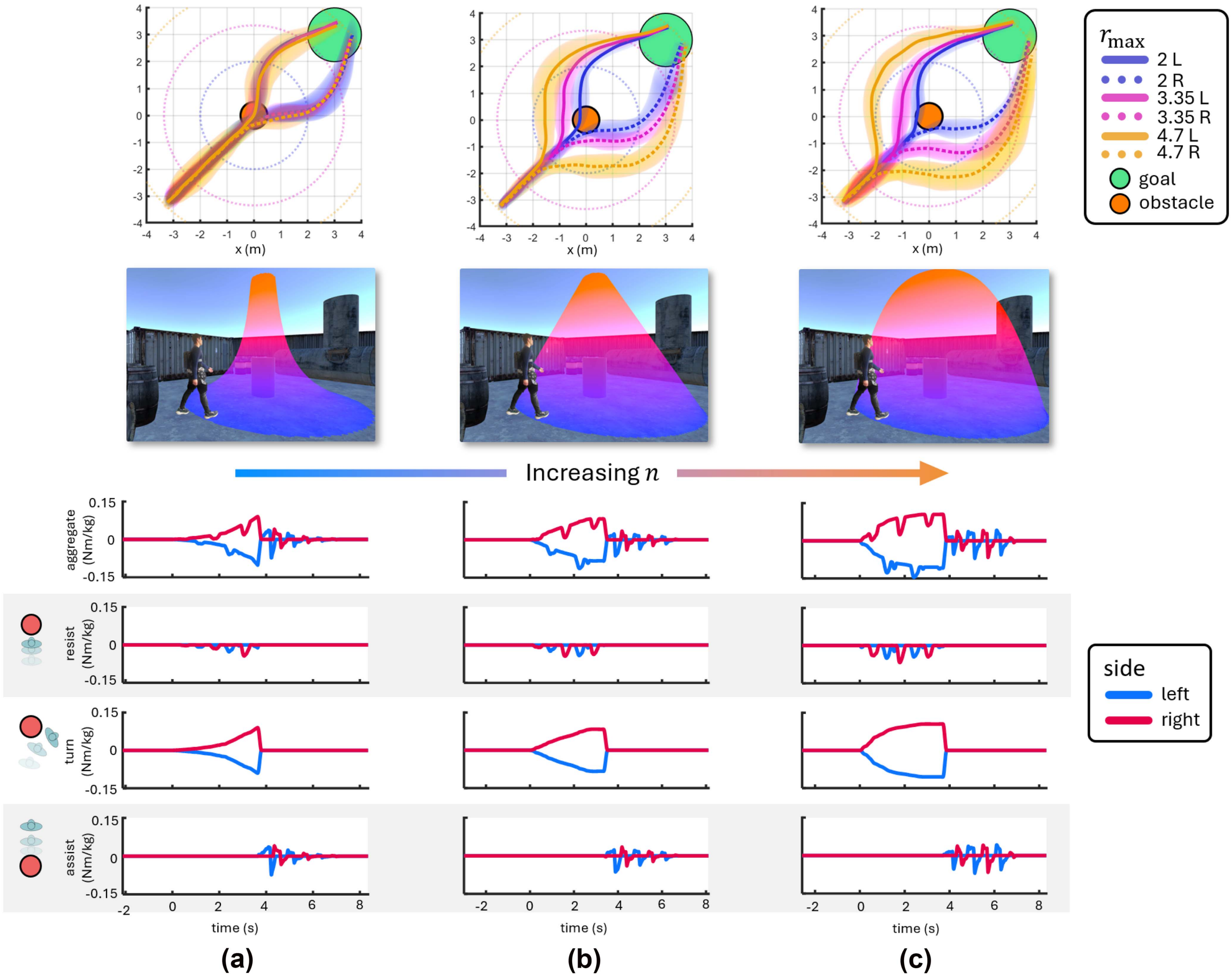

Fig. 5. (Top) X-Y trajectories for every combination of maximum radius of influence, $r_{\max}$, and fractional order, n. (a) $n = 1$. (b) $n = 3$. (c) $n = 5$. Solid and dashed lines represent conditions where the turning controller was biased left (CCW) or right (CW), respectively. A subject radius of 0.2m was used. The path outlines represent a ± 1 standard deviation. Dotted lines enclose the obstacle's area of influence. Data were averaged across subjects (N=5) and trials (M=3). A moving average filter of window size 200ms was applied to each trial for plotting purposes. (Bottom) The averaged trajectories' torque profiles for each fractional order are shown, listed in the following order: aggregate, resistive, turning, assistive.

(Fig. 4(b)), so it was ultimately selected for use in the subsequent experiments.

B. Fractional Repulsive Field

Conventionally, repulsive potential fields model an agent and obstacles in the environment as point charges in a Coulomb potential field, where the potential is inversely proportional to the square of the distance between the particles. In this model, the gradient of the potential field is lowest near an obstacle's maximum radius of influence, $r_{\max}$, and increases up to the obstacle's radius, $r_{\min}$. Early pilot experiments suggested that subjects had difficulty resolving low-magnitude exoskeleton torques near the boundary of an obstacle's area of influence. Reactions to the commanded exoskeleton torque were not observed until the torque exceeded 2 Nm, reducing the *effective* radius of influence by up to 3X ($r_{\min} = 0.5$ m, $r_{\max} < 4$ m). As a result, subjects were afforded less than one stride to react before colliding with obstacles. Because it is difficult for humans to alter their velocity mid-swing phase, the outcome of each trial (i.e., collision or no collision) was often attributed to whether or not the subject entered the effective radius of influence in double-stance.

Instead, we utilized the normalized Weyl fractional potential formulation to alter the shape of the potential curve using the fractional order n (7) [28], [29], [30].

$$U_n(r) = \frac{r^{n-2} - r_{\max}^{n-2}}{r_{\min}^{n-2} - r_{\max}^{n-2}}, \quad 1 \leq n \leq 5 \tag{7}$$

Continuously increasing n progressively alters the curve shape such that a larger value of n always results in a larger potential for any fixed distance $r \in (r_{\min}, r_{\max})$ (Fig. 6). The larger the n, the more the field behaves like a step function at $r_{\max}$. We also used this formulation to introduce obstacles of varying danger levels, where larger fractional orders correspond

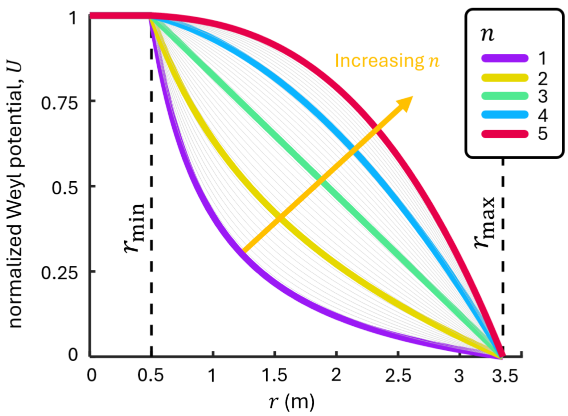

Fig. 6. Repulsive potential field shape of the normalized Weyl fractional potential formulation for $1 \leq n \leq 5$.

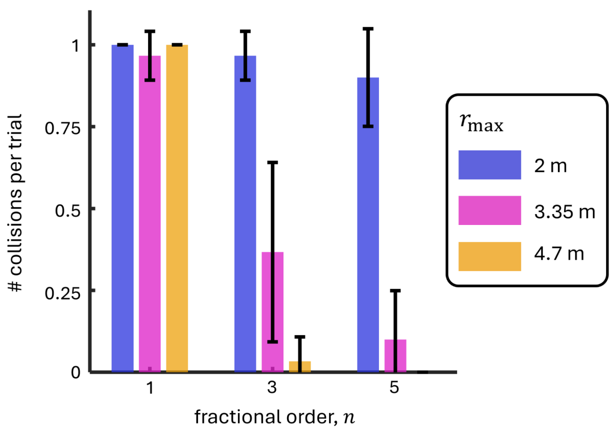

Fig. 7. A comparison of the number of collisions observed per trial, averaged across subjects for all tested n and r_{max}. The error bars represent the standard deviation of the between-subject means.

with more dangerous threats that demand a more immediate response.

We conducted an N=5 pilot study to identify a range of fractional orders large enough to elicit a quick response from the wearer while minimizing the abruptness of the produced torque commands (characteristic of very small or very large n). A single obstacle ($r_{min} = 0.5$) was simulated in virtual reality and placed at the (0,0) coordinate (middle) of an 8 x 8m field. Subjects started at the coordinates (-3, -3) and were instructed to walk directly towards a goal at coordinates (3, 3), responding to the exoskeleton torque accordingly. Subjects were unable to see the obstacle's position and did not receive feedback if a collision occurred. The turning controller was programmed to bias the wearer right (CW) or left (CCW) to eliminate the ϕ_{safe} discontinuity that occurs when $\phi_{obstacle} = 0$. Three values of r_{max} (2.0m, 3.35m, 4.7m) and three values of n (1, 3, 5) were tested for a total of 18 $(2 \times 3 \times 3)$ conditions (Fig. 5). Three trials were conducted for each condition. The overall trial order was randomized.

We found that fractional orders of $\{3, 5\}$ resulted in fewer collisions than orders of 1 for a constant r_{max} (Fig. 7). Therefore,

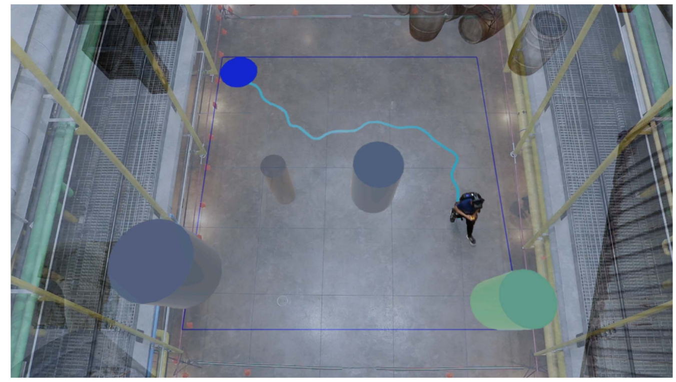

Fig. 8. A visualization of the virtual reality environment overlapped with the physical experimentation space. The subject's path is outlined in light blue. The obstacles are shown in gray. The start and goal are the blue circle and green cylinder, respectively.

we limited the range of n to [3,5] m. We also set the difference $r_{max} - r_{min}$ to 2.85m $(3.35 - 0.5)$ for follow-up experiments to provide wearers with enough space to evade the obstacles while simultaneously keeping the area of influence of each obstacle to a practical minimum. This was done to increase the number of obstacles that could reasonably fit in our environment. Tuned parameters are listed in Table I.

IV. Methods

A. Virtual Reality Platform

The obstacles and environment were simulated in virtual reality to (1) eliminate the risk of personal injury due to collisions, and (2) increase the repeatability of obstacle placement. The explorable environment consisted of a smooth, level ground terrain of size 8 x 8 m. The environment, obstacle map, and potential field were simulated in the Unity game engine, hosted on a virtual reality (VR) computer (Fig. 8). ϕ_{safe}, $\phi_{obstacle}$, and $U(x, y)$ were computed on the VR computer and transmitted to the exoskeleton over Wi-Fi via a network socket. The HTC VIVE Pro 2 VR platform with four base stations, equipped with a wireless adaptor, was used to relay video to the wearer. A VIVE tracker positioned on the back of the exoskeleton's electronics backpack was used to obtain the (x, y) coordinates of the wearer (Fig. 9).

B. Level Design

Early pilot studies revealed that subjects were memorizing the obstacle placement of select levels after repeated exposure. To minimize learning effects, one level set was generated for each degree of visibility (for a total of four level sets, to be shared across all subjects). In this experimental design, subjects are only exposed to each level twice- once with exoskeleton feedback (exo on) and once without (exo off). This method allows us to retain the ability to directly compare the exo on vs. exo off conditions while making it harder for subjects to rely on memorization. To add additional variety and complexity to each level set, we generated levels with 0, 2, 3, and 4 obstacles.

TABLE I
CONTROLLER PARAMETER SELECTION

	Parameter	Value	Units	Description
Resistive Controller	β	1.39×10^{-3}	Nm/kg/°/s	damping coefficient
Assistive Controller	α	0.6	-	spring contribution
	k	3.3×10^{-3}	-	flexion spring constant
		9.2×10^{-3}	-	extension spring constant
	θ_{eq}	53.54	%	flexion equilibrium angle $\rightarrow$ ROM[a]
		-45.78	%	extension equilibrium angle $\rightarrow$ ROM[a]
Turning Controller	τ_{diff}	0.25	Nm/kg	maximum torque
	γ	5	-	tanh shaping parameter
Fractional Repulsive Field	n_k	$\in \{3, 4, 5\}$	-	k^{th}-obstacle fractional order
	$r_{\text{k,min}}$	$\in \{0.25, 0.5, 0.75\}$	m	k^{th}-obstacle radius
	$r_{\text{k,max}}$ - $r_{\text{k,min}}$	2.85	m	k^{th}-obstacle effect radius

[a] Hip angles are mapped to % range of motion (% ROM) to account for between-subject variance kinematics.

Fig. 9. The sensors and wearable devices worn by subjects during the experiment.

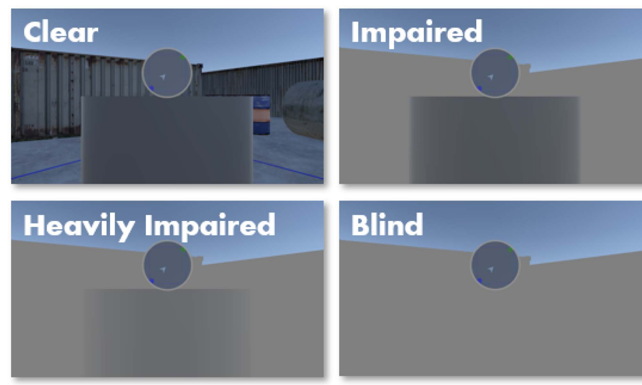

Fig. 10. Fog density comparison. The camera was positioned 0.5 m away from the edge of an obstacle, $r_o = 0.5$ m. The minimap, centered in each panel, was present solely to communicate the position of the goal.

Each level set contained 5X 2-obstacle, 5X 3-obstacle, 5X 4-obstacle, and 1X 0-obstacle levels for a total of 16 levels. The 0-obstacle catch trial was introduced to discourage subjects from anticipating path deviations.

During level generation, obstacles were randomly assigned one of three *danger* levels. The danger level was visually represented by r_{min}, where values of 0.25, 0.5, and 0.75m correspond with mild, moderate, and severe danger levels, respectively. The danger level was also linearly mapped to a repulsive potential fractional order such that mild, moderate, and severe obstacles generate repulsive fields with $n = 3, 4, 5$, respectively. Obstacle placements were then sampled from the explorable space and tested to ensure that they satisfied the following criteria:

1) The start and the goal are safe (i.e., zero potential).
2) Obstacles do not overlap. Repulsive fields are allowed to overlap, in which case the maximum potential is used.
3) There is at least one obstacle along the path from the start to the goal. This ensures that levels cannot be navigated naively, adding complexity to the task. The catch trial is the sole exception to this rule.
4) The level should be traversable by an ideal agent using gradient descent. This ensures that levels completed are not impossible.

To encourage a diverse set of trajectories in each level set, we introduced a dissimilarity index. For any two ideal agent trajectories p_i and p_j (each re-sampled to a length of 1000 timesteps), the level dissimilarity was computed using the lock-step Euclidean distance, $d(p_i, p_j)$. The larger the dissimilarity index, the more different the two levels. The level set similarity index for the k^{th} level set, s_k, was defined using (8), where $m = 16$ is the number of levels.

$$s_k = \sum_{i=1}^{m} \sum_{\substack{j=1 \\ j \neq i}}^{m} d(p_i, p_j) \tag{8}$$

We generated 100 candidate level sets and selected the set with the largest dissimilarity index. We repeated this process four times (once per visibility) to obtain the final level sets.

C. Visibility

The proposed controller was evaluated at four degrees of visibility, adjusted using Unity's built-in fog renderer in exponential squared mode (Fig. 10). The larger the fog density ρ, the more obscured the visibility:

- *Clear:* All game objects are completely visible. $\rho = 0$.
- *Impaired:* The goal and the obstacles are only visible when the subject is ~ 1.3 m away. $\rho = 2$.

- *Heavily Impaired:* The goal and the obstacles are only visible when the subject is ~ 0.8 m away. $\rho = 4$.
- *Blind:* Neither the obstacles nor the goal is rendered in the VR headset. $\rho = \infty$.

A minimap was made available to the wearer to indicate the position of the goal relative to their heading for every condition. Obstacles were not rendered on the minimap. The minimap was a necessary inclusion for conditions in which the position of the goal was not discernible through the fog.

D. Performance Evaluation Metric

Subject performance was evaluated using a derived exposure risk metric called the health score, where the damage taken at each timestep is dependent on the subject's proximity to obstacles in the field (9).

$$h_0 = 100$$
$$h_{i+1} = h_i - G \sum_{k=1}^{\#\text{obstacles}} r_{o,k} \frac{1}{r_k^2} \tag{9}$$

The health score was designed to be a continuous metric capable of providing participants with a clear, quantitative measure to maximize during both training and experiments. The damage calculation was based on the inverse square law, characteristic of radiation emissions from natural hazards such as fires, explosives, and radioactive materials. The overall damage taken by a singular obstacle is mathematically equivalent to integrating the inverse square of the subject's distance to the obstacle with respect to elapsed time. Therefore, it is possible to lose health gradually by remaining still, though it depletes much faster the closer a participant is to the obstacle. Though the health score is inherently different from the number of collisions metric (in that datapoints are not discrete), collisions were still programmed to result in an immediate depletion of health.

The damage taken by each obstacle is also proportional to its hazard level, represented by the obstacle radius $r_{o,k}$. A damage gain of $G = 0.07$ was used for the study. To provide a useful interpretation of the performance metric, we compare it to a minimum separation metric, defined as the closest distance between the participant and an obstacle during a level.

E. Experimental Protocol

Ten able-bodied subjects were recruited for the study approved by the Georgia Tech Institutional Review Board (IRB H18272). The number of subjects was calculated a-priori using a power analysis ($\alpha = 0.05$, $\beta = 0.8$) based on our pilot data. The experiment spanned two days: a training day and a data collection day. On training day, participants were given two minutes of unconstrained level ground walking acclimation for each of the three exoskeleton controllers. Next, participants were trained to navigate sample levels with real-time health feedback in each of the four visibility conditions. 12 sample levels were generated exclusively for training using the same process as the collection levels. Participants completed two sets of 12 levels—first without and then with the exoskeleton. Finally, participants completed 8 randomly-selected sample levels (one for each combination of condition and visibility) without the use of the real-time health bar; instead, the final health was revealed upon completion of the level. This ensured that subjects did not receive additional information about the locations of obstacles from the damage rate of the health bar. On average, the training portion of the protocol 2.5 hours, including breaks.

On collection day, subject performance was evaluated (1) with and without exoskeleton feedback and (2) under four degrees of visual occlusion. The blind condition with exoskeleton feedback was only conducted on the last four subjects. The blind condition without exoskeleton feedback was not evaluated because, based on the rules of obstacle generation, collisions are guaranteed for subjects taking the naive path in all but the control level. Each of the seven conditions contained 16 trials, for a total of 112 trials. As in the final session of the training day, the health score was revealed only after completing each level. The condition order was randomized, and the level/trial order was randomized within each condition. Conditions were separated by at least a 3-minute break, with a longer 10-minute break after the first four conditions. The health metric, X-Y position, global heading, kinematics, controller states, and reference torques were logged. On average, the collection lasted 3.8 hours, including breaks.

F. Statistical Analysis

Differences in performance across exoskeleton conditions and visibilities were analyzed for each metric using a repeated-measures ANCOVA, with the controller status (exo on, exo off) and visibility as within-subject factors, and condition order as a covariate to account for potential fatigue effects. If statistical significance was detected, post-hoc pairwise comparisons were conducted between exo on and exo off conditions at each visibility level, using Tukey's HSD test to account for multiple comparisons. Differences between visibilities were expected by design, and so were not included in the analysis. All statistical analyses were performed in MATLAB 2024a using a significance threshold of $\alpha = 0.05$.

V. Results

A small subset of the trajectories is shown in Fig. 11. Video demonstrations of the experiment can be found at [31]. All results are shown in Table II.

The ANCOVA tests revealed significant main and interaction effects for every metric except walking speed, for which only the interaction effect was significant. Furthermore, using condition order as a covariate, there is no statistical evidence that differences in performance manifested due to either fatigue or learning.

A. Health Score and Minimum Separation

Exoskeleton feedback significantly increased final health scores in every visibility except clear, in which significance was not detected (Fig. 12(a)). This trend was also observed within every subject (Fig. 13). Interestingly, between-subject performance in the exo on condition appeared to plateau after

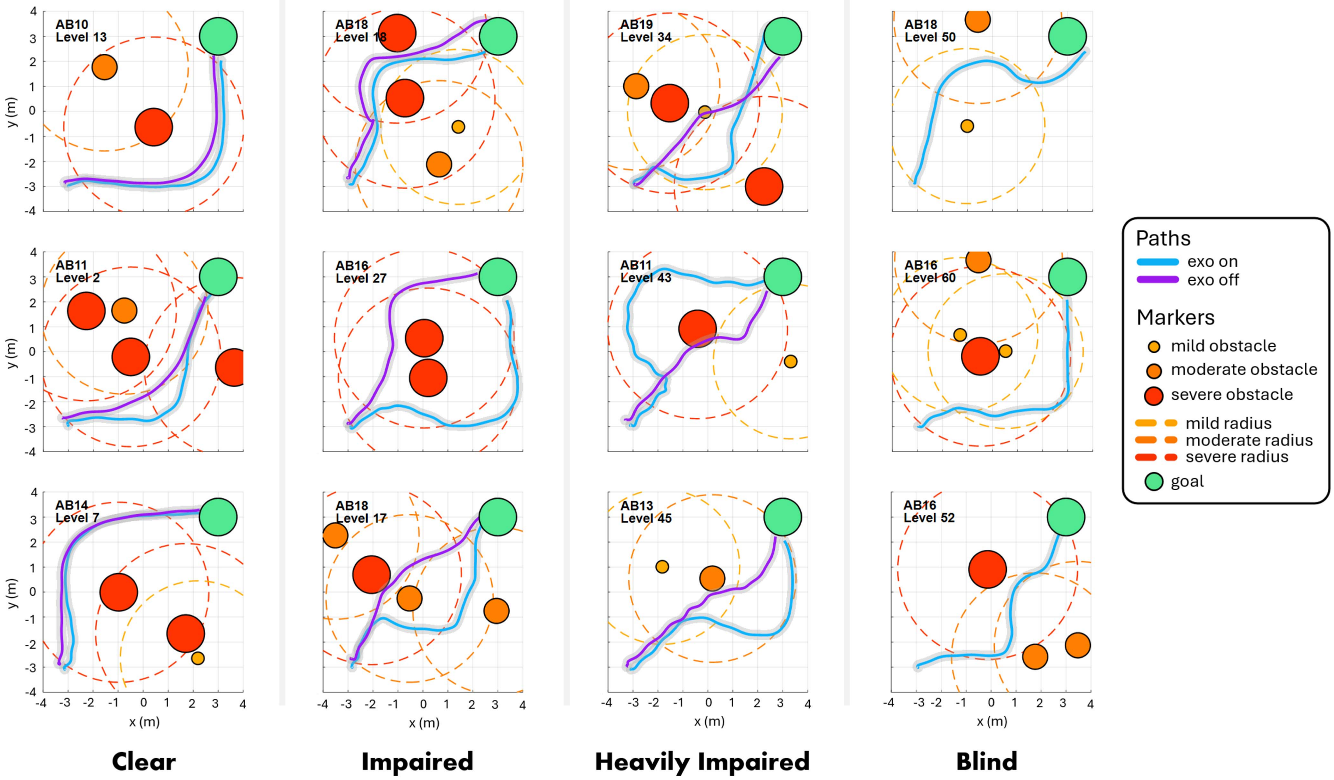

Fig. 11. X-Y trajectories for a random selection of trials. A moving average filter of window size 200 ms was applied to each trial for plotting purposes. The obstacle colors yellow, orange, and red correspond to obstacles of mild, moderate, and severe danger levels, respectively. (a) Clear. (b) Impaired. (c) Heavily impaired. (d) Blind (exo on only).

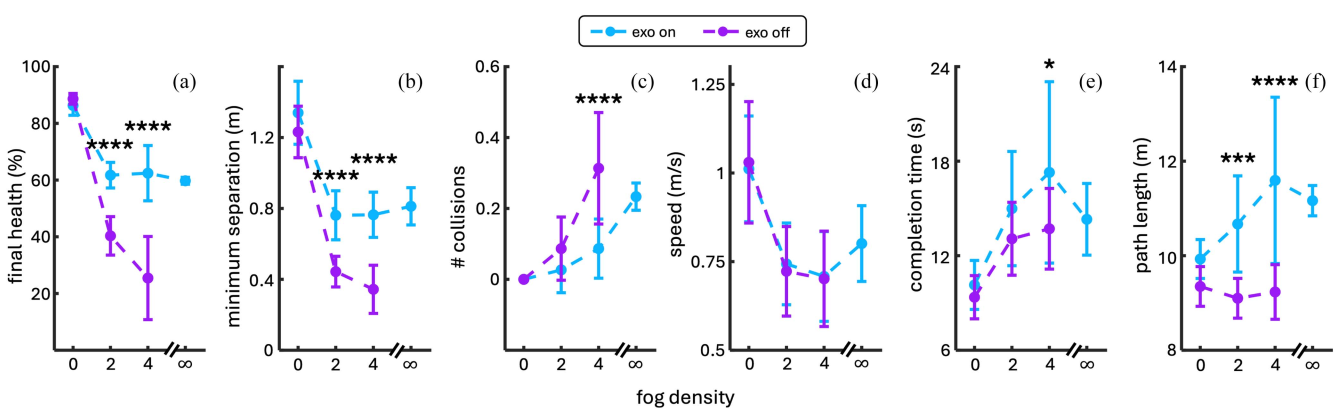

Fig. 12. Comparison of average subject performance at different visibility levels. Error bars represent the standard deviation of the between-subject performance. (a) Final health. (b) Minimum separation. (c) Number of collisions. (d) Average speed. (e) Level completion time. (f) Path length. Asterisks indicate statistical significance between conditions, where $p < 0.05$ (*), $p < 0.01$ (**), $p < 0.001$ (***), $p < 0.0001$ (****). Only four subjects constitute the $\rho = \infty$ datapoint.

the impaired visibility condition. We evaluated this hypothesis by performing another set of pairwise comparisons between visibilities for each exo condition, using Tukey's HSD test to control for multiple comparisons. Significance was detected between clear and impaired ($p < 0.0001$), clear and heavily impaired ($p < 0.0001$), and clear and blind ($p < 0.0001$), but not between any of the impaired visibility conditions. This suggests that subject performance plateaus after $\rho = 2$ in the exo on conditions.

Furthermore, exoskeleton feedback significantly increased the minimum separation compared to the exo off condition in both impaired visibility conditions, with no significance detected in the clear condition (Fig. 12(b)).

Finally, we found that the minimum separation was highly correlated with the final health scores. We performed regression using an asymptotic regression model and found r-squared values of 0.75, 0.68, and 0.73 for the clear, impaired, and heavily impaired visibilities, respectively. We also computed an

TABLE II
SUMMARY OF RESULTS

		Exo Off	Exo On	p-values^a
Metric	Fog	Mean ± Std	Mean ± Std	exo t-Test^b
Final Health (%)	0	88.7 ± 1.9	86.3 ± 3.5	0.56
	2	40.3 ± 6.8	61.7 ± 4.5	**<0.0001**
	4	25.5 ± 14.7	62.4 ± 9.7	**<0.0001**
	∞	—	59.8 ± 1.2	—
Minimum Separation (m)	0	1.23 ± 0.15	1.40 ± 0.18	0.09
	2	0.44 ± 0.09	0.76 ± 0.14	**<0.0001**
	4	0.34 ± 0.14	0.76 ± 0.13	**<0.0001**
	∞	—	0.81 ± 0.11	—
Number Collisions	0	0 ± 0	0 ± 0	—
	2	0.09 ± 0.09	0.03 ± 0.06	0.10
	4	0.31 ± 0.16	0.09 ± 0.08	**<0.0001**
	∞	—	0.23 ± 0.04	—
Walking Speed (m/s)	0	1.03 ± 0.17	1.01 ± 0.15	0.80
	2	0.72 ± 0.13	0.74 ± 0.12	0.83
	4	0.70 ± 0.13	0.71 ± 0.13	0.87
	∞	—	0.80 ± 0.11	—
Completion Time (s)	0	9.4 ± 1.4	10.1 ± 1.6	0.66
	2	13.3 ± 2.3	15.0 ± 3.6	0.12
	4	13.6 ± 2.6	17.3 ± 5.8	**0.02**
	∞	—	14.3 ± 2.3	—
Path Length (m)	0	9.3 ± 0.4	9.9 ± 0.4	0.19
	2	9.1 ± 0.4	10.7 ± 1.0	**0.0001**
	4	9.2 ± 0.6	11.6 ± 1.8	**<0.0001**
	∞	—	11.2 ± 0.3	—

^{a}Bolded p-values indicate statistical significance for $\alpha = 0.05$.
^{b}Only the comparisons between the exo on and exo off conditions within each visibility are represented by the exo t-Test to focus on the effects the exoskeleton. Differences between visibilities are expected by design.

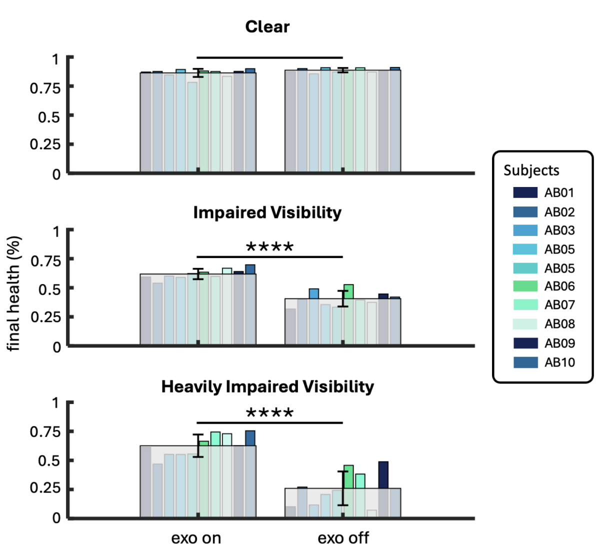

Fig. 13. Health scores averaged within (colored bars) and between (translucent) bars for different levels of visibility. Error bars represent the standard deviation of the between-subject performance. Asterisks indicate statistical significance between exo on and exo off conditions, where $p < 0.05$ (*), $p < 0.01$ (**), $p < 0.001$ (***), $p < 0.0001$ (****).

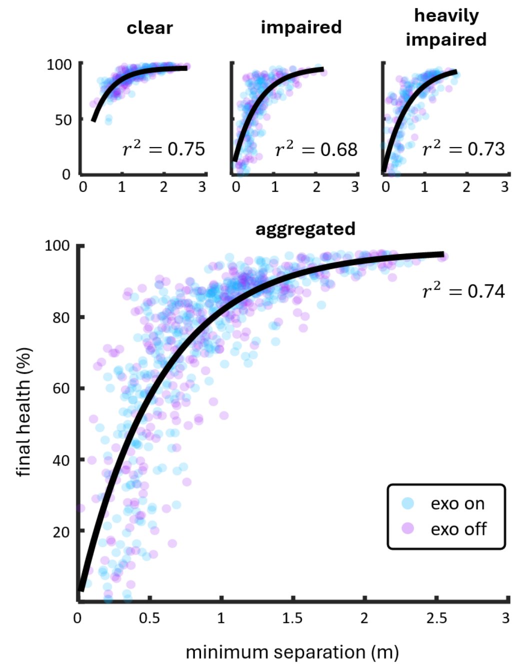

Fig. 14. A comparison between the final health and the minimum separation using every datapoint. The top row illustrates this relationship for the clear, impaired, and heavily impaired visibilities, respectively. The bottom plot is an aggregate of all trials, including the blind condition. Regression analysis was also performed, using an exponential asymptotic model with equation $y = a(1 - e^{-bx})$. Since the health score is not continuous at zero, trials with zero health were not used for the regression.

r-squared value of 0.74 for the aggregated dataset (Fig. 14), which indicates a strong correlation.

B. Collisions

The average number of collisions observed in every trial increased with increasing fog density. In the impaired visibility conditions, exoskeleton feedback significantly decreased the average number of collisions per level (Fig. 12(c)).

C. Trajectory Metrics

Exoskeleton feedback did not appear to affect walking speed, but significantly increased path lengths in the impaired visibilities (Fig. 12(d), (f)). Completion times were not significantly increased by exoskeleton feedback for all but the heavily impaired condition, for the exo significantly increased completion time (Fig. 12(e)).

VI. DISCUSSION

A. Performance Assessment

Our findings suggest that the proposed control framework is a viable and effective method for reducing operator exposure to danger in environments with poor visibility. Significant performance improvements, as measured by the final health score, were observed when the controller was enabled in each of the reduced visibility conditions. While there is no real-world interpretation of the health score, we can derive a protocol-specific interpretation by using it as a predictor of minimum separation from obstacles, where a strong correlation was observed. Exoskeleton feedback also reduced the average number of collisions by over threefold in each of the impaired visibility conditions. This suggests potential safety benefits for workers in hazardous environments, distracted individuals, and/or visually impaired populations, though additional work is necessary to test each of these hypotheses.

The lack of significant difference in exposure risk in the impaired visibility exo conditions also deviated from our expectation that performance would worsen as visibility decreased. We believe this occurred because participants mostly relied on exoskeleton feedback rather than visual cues for navigation. This is likely a consequence of the decision to make the obstacles' effect radius larger than the range of visibility. We hypothesize that a correlation between visibility and final health exists between visibilities $\rho = 0$ and $\rho = 2$. Despite this, our findings suggest that subjects were able and willing to accept the suggested routing, even at the lowest visibility level.

Curiously, the exoskeleton largely did not affect participant walking speeds in any of the visibility conditions. We hypothesized that this occurred because potential increases in walking speed enabled by the assistive controller were counteracted by the resistive and turning controllers. To test this hypothesis, we isolated parts of the trials where the assistive controller was active (i.e., when participants were moving away from obstacles) and computed average walking speeds for each. We then computed the relative increase in walking speed compared to the remainder of the trial. We compared the difference in the exo on condition to that in the exo off condition to determine if the increase in speed was attributable to the controller or the user (based on the observation that they cleared the last obstacle). We determined that, in the exo on conditions, participant walking speeds increased by 29.7% compared to 19.1% in the exo off conditions. However, it is unclear if this difference was a consequence of biomechanical assistance or a feedback mechanism informing the wearer that they cleared the obstacle. Finally, is also unclear if any further increases in self-selected walking speed were offset by the weight and inertia of the device. It is possible that a lighter platform may have resulted in more pronounced increases in walking speed.

Lastly, the trajectory analysis results show that path lengths were longer on average with exoskeleton feedback compared to without. This behavior likely stems from the exoskeleton suggesting safer paths, which required larger deviations from the direct route. Supporting this, we observed (1) increased trial completion times on average, despite mostly unaffected average speeds, and (2) greater separation from obstacles when the controller was active. This is a reasonable trade-off, as the controller was designed to prioritize safety over path efficiency.

B. Experimental Limitations

An investigation into failed trials (i.e., $h_{\text{end}} = 0$) revealed that the two leading causes of collisions for the exo on conditions were (1) navigating into local minima and (2) being pushed out of bounds (Fig. 16).

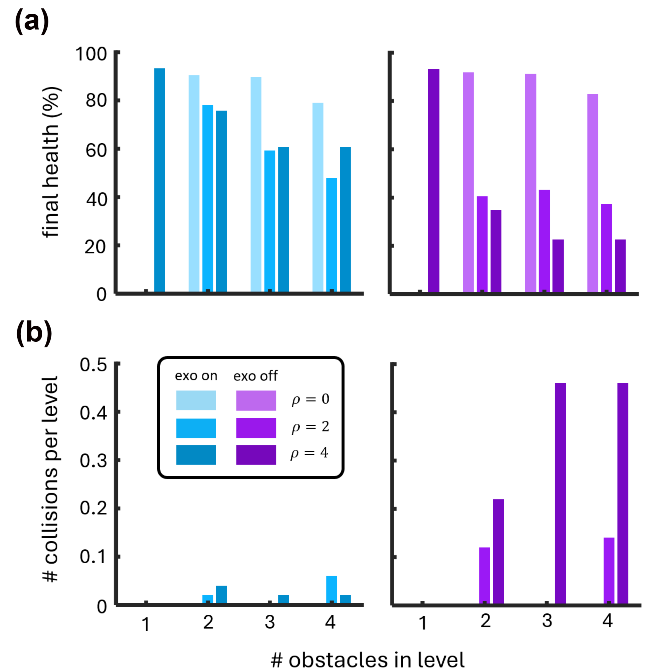

Fig. 15. A comparison of (a) the average final health scores for different visibilities and (b) the average number of collisions per level, grouped by the numbers of obstacles per level. Data from the repulsive field tuning pilot study were used for the 1-obstacle bar since the experiment did not contain any levels with a singular obstacle. No statistics were performed.

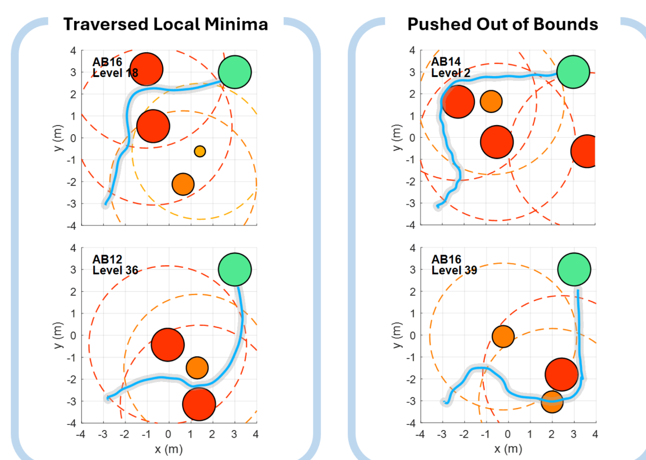

Fig. 16. Examples of common failure modes. Trajectories are a hand-picked subset of all occurrences.

1) Local Minima: Local minima occurred when the repulsive fields of two obstacles overlapped, causing repulsion of equal magnitude in opposite directions. At these points, the discontinuity in ∇U caused jumps in ϕ_{safe}, resulting in mixed exoskeleton feedback. Though experienced users in pilot studies were able to consistently identify these minimums as valid paths, less experienced participants occasionally reported some confusion. We can infer a similar story from the data, where participant performance decreased in levels with higher obstacle counts (Fig. 15), apparent from the inverse relationship between final health scores and the number of obstacles per level in the exo on conditions. Since the same relationship is not as prominent in the exo off conditions, we believe it is best explained by non-intuitive exoskeleton feedback in the presence of multiple obstacles. This suggests that the current implementation of the controller may not be optimal for close-quarters navigation.

Local minima are a well understood failure mode of artificial potential fields, which have known solutions including:

- implementing a homeomorphism to transform the potential surface into one with no local minimums [32].
- defining ϕ_{safe} using a method other than gradient descent.

Though we sought to demonstrate the effectiveness of this approach using the simplest and most general form of artificial potential fields, we believe future implementations could benefit from implementing one of the aforementioned solutions or utilizing a comparable navigation algorithm.

2) Out of Bounds: The out-of-bounds problem resulted from the space limitations imposed by the virtual reality platform. Subjects reported receiving turning commands directing them to overshoot the field boundary, in which case they expressed having no choice but to ignore the suggested direction (often resulting in a collision). One considered solution was to define the boundaries as repulsive obstacles, but this idea was rejected because (1) the effective safe space would be very small and (2) it would exacerbate the local minimum problem for obstacles near the boundary. We believe that this effect would be less pronounced in a setting where wearers are less concerned about experimental boundaries.

C. Design Limitations

The most apparent limitation of the proposed design is its reliance on precise obstacle and wearer positions. In structured environments like warehouses or construction zones, this can be accomplished by using mounted cameras or co-robots. However, this is often neither feasible nor practical, especially in unstructured environments. In these instances, we propose leveraging egocentric sensing methods to assist with mapping and planning. Research in wearable robotics has already demonstrated the feasibility of using cameras [33], [34], [35], [36] and LiDAR [36] to aid in navigation; we intend to incorporate both in our future work. Another limitation of this design is the choice of only actuating a single joint. We selected a single-joint platform to (1) demonstrate that the framework is effective even in exoskeletons with limited control authority and (2) be compatible with the majority of existing hip exoskeletons. Integrating this framework onto an exoskeleton platform that supports multiple degrees of freedom could more accurately reproduce human dynamics during obstacle evasion. Furthermore, the current implementation of the assistive impedance controller utilizes parameters derived from the biomechanics of level-ground walking at a speed of 1.25 m/s. This walking speed proved to be an incorrect assumption, as people chose to walk slower in these environments (Fig. 12(d)). A continuous controller that adapts to other walking speeds and ambulation modes can better model the hip's dynamics [37]. Finally, in scenarios where the suggested direction conflicts with the user's intent, the controller should be designed to adapt as needed. The simplest solution to this dilemma is to disable the controller if the heading error increases over some time horizon. At a minimum, a physical override button should be present.

VII. Conclusion

As actuator technology and real-time sensing capabilities continue to improve, wearable exoskeletons are likely to become more viable for use in dynamic workplaces. We believe that the addition of a collision avoidance controller can be very conducive to increasing worker safety. In this paper, we present a first-of-its-kind controller for human navigation and demonstrate evidence of its effectiveness through a series of human-subject experiments. Our health score results indicate that the exoskeleton provides significant benefits to vision alone in conditions where visibility is limited to a range of $\sim$ 1.3m ($p < 0.0001$) and $\sim$ 0.8m ($p < 0.0001$). The number of collisions observed was reduced by $\sim$3Xand $\sim$3.4X in the impaired and heavily impaired visibility conditions, respectively. These results indicate that providing force-feedback in parallel with a human is an effective strategy to improve overall navigation ability in low visibility environments, requiring minimal training and no subject-specific tuning. Future work is necessary to incorporate onboard sensors and refine this control paradigm for real-world navigation with dynamic obstacles. Additionally, comparative studies could examine performance differences between the proposed force-feedback approach and other existing haptic methods such as vibrotactile and upper limb feedback. We are hopeful that future applications of this work may include completely blind navigation (i.e., where the exact position of the goal is not known) for both healthy and clinical populations.

Acknowledgment

The authors would like to thank Connor Bossard, Ryan Casey, Joshua Fernandez, and Marilyn Braojos for their contributions to the ideation and development of the project. The authors would also like to thank all of the participants who volunteered their time to make this work possible.

References

[1] "Top work-related injury causes-data details," 2021. [Online]. Available: https://injuryfacts.nsc.org/work/work-overview/top-work-related-injury-causes/data-details/

[2] "Effects of visual, auditory, and tactile navigation cues on navigation performance, situation awareness, and mental workload," Tech. Rep., section: Technical Reports, Jan. 2007. [Online]. Available: https://apps.dtic.mil/sti/citations/ADA463244

[3] A. Bajpai, J. C. Powell, A. J. Young, and A. Mazumdar, "Enhancing physical human evasion of moving threats using tactile cues," *IEEE Trans. Haptics*, vol. 13, no. 1, pp. 32–37, Jan.–Mar. 2020. [Online]. Available: https://ieeexplore.ieee.org/document/8943999

[4] J. B. F. V. Erp, H. A. H. C. V. Veen, C. Jansen, and T. Dobbins, "Waypoint navigation with a vibrotactile waist belt," *ACM Trans. Appl. Percep.*, vol. 2, no. 2, pp. 106–117, Apr. 2005. [Online]. Available: https://dl.acm.org/doi/10.1145/1060581.1060585

[5] A. Carton and L. E. Dunne, “Tactile distance feedback for firefighters: Design and preliminary evaluation of a sensory augmentation glove,” in *Proc. 4th Augmented Hum. Int. Conf.*, Mar. 2013, pp. 58–64. [Online]. Available: https://dl.acm.org/doi/10.1145/2459236.2459247

[6] A. Bajpai, K. M. Feigh, A. Mazumdar, and A. J. Young, “Influencing human escape maneuvers with perceptual cues in the presence of a visual task,” *IEEE Trans. Hum.-Mach. Syst.*, vol. 51, no. 6, pp. 715–724, Dec. 2021. [Online]. Available: https://ieeexplore.ieee.org/document/9540710

[7] H. Kerdegari, Y. Kim, and T. J. Prescott, “Head-mounted sensory augmentation device: Designing a tactile language,” *IEEE Trans. Haptics*, vol. 9, no. 3, pp. 376–386, Jul.–Sep. 2016. [Online]. Available: https://ieeexplore.ieee.org/document/7452615

[8] J. Rosenthal, N. Edwards, D. Villanueva, S. Krishna, T. McDaniel, and S. Panchanathan, “Design, implementation, and case study of a pragmatic vibrotactile belt,” *IEEE Trans. Instrum. Meas.*, vol. 60, no. 1, pp. 114–125, Jan. 2011. [Online]. Available: https://ieeexplore.ieee.org/abstract/document/5659690

[9] Y. Salzer, T. Oron-Gilad, A. Ronen, and Y. Parmet, “Vibrotactile On-thigh” alerting system in the cockpit,” *Hum. Factors*, vol. 53, no. 2, pp. 118–131, Apr. 2011. [Online]. Available: https://doi.org/10.1177/0018720811403139

[10] A. Meier, D. J. C. Matthies, B. Urban, and R. Wettach, “Exploring vibrotactile feedback on the body and foot for the purpose of pedestrian navigation,” in *Proc. 2nd Int. Workshop Sensor-Based Activity Recognit. Interaction*, Jun. 2015, pp. 1–11. [Online]. Available: https://dl.acm.org/doi/10.1145/2790044.2790051

[11] J. R. Blum et al., “Getting your hands dirty outside the lab: A practical primer for conducting wearable vibrotactile haptics research,” *IEEE Trans. Haptics*, vol. 12, no. 3, pp. 232–246, Jul.–Sep. 2019. [Online]. Available: https://ieeexplore.ieee.org/document/8770138

[12] P. Slade, A. Tambe, and M. J. Kochenderfer, “Multimodal sensing and intuitive steering assistance improve navigation and mobility for people with impaired vision,” *Sci. Robot.*, vol. 6, no. 59, Oct. 2021, Art. no. eabg6594. [Online]. Available: https://www.science.org/doi/full/10.1126/scirobotics.abg6594

[13] M. Tognon, R. Alami, and B. Siciliano, “Physical human-robot interaction with a tethered aerial vehicle: Application to a force-based human guiding problem,” *IEEE Trans. Robot.*, vol. 37, no. 3, pp. 723–734, Jun. 2021. [Online]. Available: https://ieeexplore.ieee.org/abstract/document/9353246

[14] “DOE evaluates wearable robotic devices to aid cleanup workforce,” Nov. 2022. [Online]. Available: https://www.ans.org/news/article-4476/doe-evaluates-wearable-robotic-devices-to-aid-cleanup-workforce/

[15] M. A. Nussbaum, B. D. Lowe, M. de Looze, C. Harris-Adamson, and M. Smets, “An introduction to the special issue on occupational exoskeletons,” *IISE Trans. Occup. Ergonom. Hum. Factors*, vol. 7, no. 3/4, pp. 153–162, Oct. 2019. [Online]. Available: https://doi.org/10.1080/24725838.2019.1709695

[16] A. Chu, H. Kazerooni, and A. Zoss, “On the biomimetic design of the berkeley lower extremity exoskeleton (BLEEX),” in *Proc. 2005 IEEE Int. Conf. Robot. Automat.*, Apr. 2005, pp. 4345–4352, [Online]. Available: https://ieeexplore.ieee.org/abstract/document/1570789

[17] A. Bajpai et al., “Design and validation of a versatile high torque quasidirect drive hip exoskeleton,” *IEEE/ASME Trans. Mechatron.*, vol. 29, no. 1, pp. 789–797, Feb. 2024. [Online]. Available: https://ieeexplore.ieee.org/document/10342739

[18] P. Malcolm, W. Derave, S. Galle, and D. D. Clercq, “A simple exoskeleton that assists plantarflexion can reduce the metabolic cost of human walking,” *PLoS One*, vol. 8, no. 2, Feb. 2013, Art. no. e56137. [Online]. Available: https://journals.plos.org/plosone/article?id=10.1371/journal.pone.0056137

[19] G. S. Sawicki, O. N. Beck, I. Kang, and A. J. Young, “The exoskeleton expansion: Improving walking and running economy,” *J. NeuroEngineering Rehabil.*, vol. 17, no. 1, Feb. 2020, Art. no. 25. [Online]. Available: https://doi.org/10.1186/s12984-020-00663-9

[20] Z. Wang et al., “A semi-active exoskeleton based on EMGs reduces muscle fatigue when squatting,” *Front. Neurorobot.*, vol. 15, 2021, Art. no. 625479. [Online]. Available: https://www.frontiersin.org/articles/10.3389/fnbot.2021

[21] P. W. Franks, G. M. Bryan, R. M. Martin, R. Reyes, A. C. Lakmazaheri, and S. H. Collins, “Comparing optimized exoskeleton assistance of the hip, knee, and ankle in single and multi-joint configurations,” *Wearable Technol.*, vol. 2, 2021, Art. no. e16. [Online]. Available: https://doi.org/10.1017/wtc.2021.14

[22] D. J. Farris and G. S. Sawicki, “The mechanics and energetics of human walking and running: A joint level perspective,” *J. Roy. Soc. Interface*, vol. 9, no. 66, pp. 110–118, May 2011. [Online]. Available: https://royalsocietypublishing.org/doi/full/10.1098/rsif.2011.0182

[23] A. E. Patla, S. D. Prentice, C. Robinson, and J. Neufeld, “Visual control of locomotion: Strategies for changing direction and for going over obstacles,” *J. Exp. Psychol.: Hum. Percep. Perform.*, vol. 17, no. 3, pp. 603–634, 1991, (n.d.) [Online]. Available: https://doi.org/10.1037/0096-1523.17.3.603

[24] G. Courtine and M. Schieppati, “Human walking along a curved path. i. body trajectory, segment orientation and the effect of vision,” *Eur. J. Neurosci.*, vol. 18, no. 1, pp. 177–190, 2003. [Online]. Available: https://onlinelibrary.wiley.com/doi/abs/10.1046/j.1460-9568.2003.02736.x

[25] H. Murakami, C. Feliciani, Y. Nishiyama, and K. Nishinari, “Mutual anticipation can contribute to self-organization in human crowds,” *Sci. Adv.*, vol. 7, no. 12, Mar. 2021, Art. no. eabe7758. [Online]. Available: https://www.science.org/doi/full/10.1126/sciadv.abe7758

[26] K. Shamaei, G. S. Sawicki, and A. M. Dollar, “Estimation of quasi-stiffness of the human hip in the stance phase of walking,” *PLoS One*, vol. 8, no. 12, Dec. 2013, Art. no. e81841. [Online]. Available: https://journals.plos.org/plosone/article?id=10.1371/journal.pone.0081841

[27] J. Camargo, A. Ramanathan, W. Flanagan, and A. Young, “A comprehensive, open-source dataset of lower limb biomechanics in multiple conditions of stairs, ramps, and level-ground ambulation and transitions,” *J. Biomech.*, vol. 119, Apr. 2021, Art. no. 110320. [Online]. Available: https://www.sciencedirect.com/science/article/pii/S0021929021001007

[28] A. Poty, P. Melchior, and A. Oustaloup, “Dynamic path planning for mobile robots using fractional potential field,” in *Proc. IEEE 1st Int. Symp. Control, Commun. Signal Process.*, Mar. 2004, pp. 557–561. [Online]. Available: https://ieeexplore.ieee.org/document/1296443

[29] P. Melchior, B. Metoui, A. Poty, S. Najar, A. Oustaloup, and M. N. Abdelkrim, “Attractive force based on fractional potential in dynamic motion planning for mobile robot,” *Amer. Soc. Mech. Engineers Digit. Collection*, vol. 4806, pp. 1423–1430, May 2009. [Online]. Available: https://dx.doi.org/10.1115/DETC2007-35495

[30] J.-B. Receveur, S. Victor, and P. Melchior, “Autonomous car decision making and trajectory tracking based on genetic algorithms and fractional potential fields,” *Intell. Service Robot.*, vol. 13, no. 2, pp. 315–330, Apr. 2020. [Online]. Available: https://doi.org/10.1007/s11370-020-00314-x

[31] C. Carrasquillo, “Enhancing human navigation ability using force-feedback from a lower-limb exoskeleton,” May 2024. [Online]. Available: https://youtu.be/gkE1IRs_Nrc

[32] E. Rimon, “Exact robot navigation using artificial potential functions,” Ph.D. dissertation, Yale Univ., New Haven, CT, USA, 1990. [Online]. Available: https://www.proquest.com/docview/303842174/abstract/8D6A0343321648BBPQ/1

[33] M. Ramanathan et al., “Visual environment perception for obstacle detection and crossing of lower-limb exoskeletons,” in *Proc. 2022 IEEE/RSJ Int. Conf. Intell. Robots Syst.*, Oct. 2022, pp. 12267–12274, [Online]. Available: https://ieeexplore.ieee.org/abstract/document/9981412

[34] M. Ramanathan, L. Luo, M. J. Foo, C. H. Chiam, W.-Y. Yau, and W. T. Ang, “Heuristic vision based terrain recognition for lower limb exoskeletons,” in *Proc. 16th Int. Conv. Rehabil. Eng. Assistive Technol.*, Jan. 2024, pp. 25–28. [Online]. Available: https://dl.acm.org/doi/10.1145/3628228.3628488

[35] J. Wang, M. Mattamala, C. Kassab, L. Zhang, and M. Fallon, “Exosense: A vision-centric scene understanding system for safe exoskeleton navigation,” Mar. 2024. [Online]. Available: https://arxiv.org/abs/2403.14320v1

[36] W. Wang, C. K. Liu, and M. Kennedy III, “EgoNav: Egocentric scene-aware human trajectory prediction,” Mar. 2024. [Online]. Available: https://arxiv.org/abs/2403.19026v3

[37] “Estimating human joint moments unifies exoskeleton control, reducing user effort science robotics,” Mar. 2024. [Online]. Available: https://www.science.org/doi/full/10.1126/scirobotics.adi8852